Pergamon

PII: S0021-8502(96)00481-8

J. Aerosol Sci. Vol. 28, No. 6, pp. 959–972, 1997

0021-8502/97 $17.00 + 0.00

A 2-D MULTICOMPONENT MODAL AEROSOL MODEL AND ITS APPLICATION TO LAMINAR FLOW REACTORS

Martin Wilck and Frank Stratmann*

Institut für Troposphärenforschung, Permoserstr. 15, 04303 Leipzig, Germany

(*First received* 29 *April* 1996; *and in final form* 29 *October* 1996)

Abstract—A multicomponent modal aerosol model suitable for two- and three-dimensional applications is introduced. Besides the moments of the size distribution, the model yields information on the time evolution of the mode-average particle composition. The model is applied to a laminar flow aerosol reactor (LFAR) problem, and the results are compared with the experiments by Nguyen *et al.* (1987) *J. Colloid Interface Sci.* **119,** 491–504 and with those of the previously published models. The influence of different model parameters is examined. The wall temperature profile is shown to be of crucial importance for LFAR simulations and experiments. For the classical nucleation rate as well as for the modified classical nucleation rate by Girshick *et al.* (1990) *Aerosol Sci. Technol.* **13,** 465–477, suitable correction factors, which give good agreement between simulation and experimental data over a wide range of experimental parameters are presented. © 1997 Elsevier Science Ltd

1. INTRODUCTION

In aerosol science, there is a strong need for aerosol dynamic models that are sufficiently simple to be applied in complex two- and three-dimensional situations and still yield reliable information about the basic properties of the resulting aerosol size distributions. Examples for such situations are atmospheric modeling or simulations of spatially inhomogeneous aerosol reactors. The modal aerosol dynamics (MAD) modeling technique (Whitby, 1989; Whitby *et al.*, 1991) is a method to calculate the dynamics of integral quantities of the size distribution with a small number of differential equations. In this technique, the size distribution is assumed to consist of distinct particle populations, called "modes", which can be represented by analytical functions. Usually, the lognormal function is employed, because it has convenient mathematical properties, and the aerosol size distributions measured can often be very well approximated by sums of lognormal distributions.

The original MAD technique does not incorporate information about particle composition. Brock *et al.* (1988) have presented a unimodal two-component model using a density function that was lognormal in two independent variables. This technique yields a lot of information on particle composition, but looses much of the speed advantage of the modal technique because single integrals have to be replaced by double integrals. The computational effort would increase exponentially if further chemical components were added.

A simple multicomponent modal modeling technique is introduced in this paper. Apart from the size-distribution parameters, it also provides information about the average chemical composition in each mode. This method requires the solution of two equations plus one additional equation per chemical component in each mode. The increase of computational effort is moderate and linear in the number of components. Based on the theory presented in this paper, the Fortran code MADMAcS 1 (multicomponent aerosol dynamics modeling—modal approach system) has been developed. At present it is used in the framework of a 2-D solver algorithm for numerical heat transfer and fluid flow problems (Patankar, 1980).

* Author to whom all correspondence should be addressed.

As a test case, the model is used to simulate a 2-D problem that has been well examined experimentally: the laminar flow aerosol reactor (LFAR). The model results are compared with the measurements of homogeneous and heterogeneous nucleation in a LFAR presented by Nguyen *et al.* (1987). To our knowledge, two other models have been used to describe these measurements before: First, the model of Peshty *et al.* (1983) was employed in the original article of Nguyen *et al.*; this is a model without *a priori* assumptions on the form of the size distribution, but, on the other hand, constrained to laminar systems with negligible radial transport. Second, a unimodal, dimensionless lognormal model was presented by Phanse and Pratsinis (1989). The results of the three models are compared with each other and to the measured data.

Recently, LFARs have been used again for nucleation studies (Anisimov *et al.*, 1994; Hämeri *et al.*, 1995); improved and efficient modeling techniques for systems of this type are therefore highly desirable for the interpretation of the experimental results.

2. THEORY

2.1. *Basics of the modal aerosol dynamics modeling technique*

The main goal of aerosol dynamics modeling is to describe the dynamics of the density function of the size distribution. In this article, the size distribution is expressed in terms of particle mass m_p; concentrations are always related to the mass of the surrounding gas. The density function $n(m_p)$ denotes the number of particles with particle mass between m_p and $m_p + dm_p$ per unit mass of gas, and its dimension is kg^{-2}.

In the modal technique, the size distribution is assumed to be the sum of distinct populations, each of which is called a "mode". The density function of each mode is described by an analytical function, usually the lognormal function. The lognormal density function of mode j is characterized by its total number concentration N_j, geometric mean mass $m_{gn,j}$ and geometric standard deviation $\sigma_{g,j}$:

$$n_{LN,j}(m_p) = \frac{N_j}{\sqrt{2\pi}\, m_p \ln \sigma_{g,j}} \exp\left(- \frac{(\ln m_p - \ln m_{gn,j})^2}{2 \ln^2 \sigma_{g,j}} \right). \tag{1}$$

The kth moment of the distribution of mode j is defined as

$$M_{k,j} = \int_0^\infty m_p^k\, n_{LN,j}(m_p)\, dm_p . \tag{2}$$

Note that $M_{0,j} = N_j$ is the total number concentration in mode j and $M_{1,j}$ is the particle mass in mode j per unit mass of the gas. $M_{0,j}$, $M_{1,j}$ and $M_{2,j}$ are used in this article to calculate the size distribution dynamics: if the values of three arbitrary moments are known, the distribution parameters N_j, $m_{gn,j}$ and $\sigma_{g,j}$ may be derived therefrom.

In aerosol dynamical processes, the particle size distribution changes due to various mechanisms, which are divided into external processes (particle transport by convection, diffusion, and external forces, e.g. sedimentation and thermophoresis) and internal processes (condensation, evaporation, homogeneous nucleation, and coagulation). The time evolution of the size distribution caused by internal as well as external processes is described by the general dynamics equation (GDE) for aerosols (see e.g. Friedlander, 1977).

In the modal approach, the GDE is transformed into a differential equation for the moments (Whitby *et al.*, 1991). The result is the moment dynamics equation (MDE), which, in the absence of coagulation and chemical reactions, has the following form:

$$\frac{\partial \rho_g M_{k,j}}{\partial t} = -\nabla \cdot (\mathbf{u}_g + \mathbf{c}_{k,j})\, \rho_g M_{k,j} + \nabla \cdot \int_0^\infty m_p^k D_p(m_p) \rho_g \nabla n_{LN,j}\, dm_p + \left(\frac{\partial \rho_g M_{k,j}}{\partial t} \right)_{cond} + \left(\frac{\partial \rho_g M_{k,j}}{\partial t} \right)_{nuc} . \tag{3}$$

In this equation, $\mathbf{u}_g$ denotes the gas velocity, ρ_g the gas density, D_p the particle diffusivity, and $\mathbf{c}_{k,j}$ stands for the kth moment average of the external particle velocity $\mathbf{c}_p$ over mode j:

$$\mathbf{c}_{k,j} = \frac{1}{M_{k,j}} \int_0^\infty \mathbf{c}_p(m_p)\, m_p^k\, n_{LN,j}(m_p)\, dm_p \,. \tag{4}$$

The particle diffusion coefficient D_p as well as the particle velocity $\mathbf{c}_p$ caused by an external force $\mathbf{F}$ can be expressed in terms of the friction coefficient f_p:

$$D_p = \frac{k_B T}{f_p}, \quad \mathbf{c}_p = \frac{\mathbf{F}}{f_p}, \quad f_p = \frac{3\pi\mu_g d_p}{C_s} \,, \tag{5}$$

where

$$C_s = 1 + \mathrm{Kn}(1.257 + 0.4e^{-1.1/\mathrm{Kn}})$$

is the slip correction factor, d_p the particle diameter, Kn the Knudsen number (mean free path of gas molecules divided by the particle radius), and μ_g the dynamic viscosity of the gas.

If $\mathbf{F}$ is, e.g. the thermophoretic force, the respective velocity can be calculated according to Talbot *et al.* (1980):

$$\mathbf{c}_{th,p} = k_{th} \cdot \frac{\mu_g}{\rho_g} \cdot \frac{\nabla T}{T}, \tag{6}$$

$$k_{th} = \frac{2.294\, C_s (k_g/k_p + 2.2\,\mathrm{Kn})}{(1 + 3.438\,\mathrm{Kn}) \cdot (1 + 2k_g/k_p + 4.4\,\mathrm{Kn})},$$

where k_g and k_p denote the heat conductivities of gas and particle, respectively.

For computational purposes, it is useful to write the diffusion term in equation (3) in the form $\nabla \cdot (\rho_g D_{k,j} \nabla M_{k,j})$ with a suitable moment diffusion coefficient $D_{k,j}$. According to Whitby *et al.* (1991), $D_{k,j}$ is calculated in the same way as $\mathbf{c}_{k,j}$ in equation (4).

2.2. *Chemical composition*

The modified modal modeling technique introduced in this article uses the same assumptions for the size distribution as in Section 2.1. Composition is taken into account by splitting the first moment $M_{1,j}$ into the contributions $M_{1,i,j}$ of the individual chemical components: $M_{1,i,j}$ denotes the total mass of species i contained in particles of mode j per unit mass of gas. Now the average mass fraction of component i in mode j can be defined as

$$\bar{\xi}_{i,j} = \frac{M_{1,i,j}}{M_{1,j}} = \frac{M_{1,i,j}}{\sum_i M_{1,i,j}} \,. \tag{7}$$

The MDE (equation (3)) can be rewritten for the "split" moments $M_{1,i,j}$ in an anologous fashion. It is important to note that convectional and external velocities as well as diffusion coefficients depend only on particle size, not on composition. Therefore, the corresponding terms in the governing equation for $M_{1,i,j}$ are identical to the first two terms on the right-hand side of equation (3). For the internal processes, on the other hand, the time evolution has to be considered for each component separately. The next subsection illustrates this for condensation and nucleation.

2.3. *Internal processes*

2.3.1. Condensation and evaporation. The rate of condensation of species i is given by (Friedlander, 1977)

$$\left.\frac{dm_{p,i}}{dt}\right|_{m_p} = 2\pi D_{m,i}\, d_p\, \xi_{v,eq,i}\, \rho_g f(\mathrm{Kn})\, (S_i - E), \quad E = \exp\left(\frac{4\sigma_p v_{m,i}}{k_B T d_p}\right). \tag{8}$$

In this equation, $D_{m,i}$ denotes the molecular diffusivity of species i, $\xi_{v,i}$ the vapor mass fraction of species i in the gas phase and $\xi_{v,eq,i}$ the equilibrium vapor mass fraction over

a flat surface, $f(\mathrm{Kn})$ the transition function (in our simulations, the formula of Fuchs and Sutugin (1971) was applied), $S_i = \xi_{\mathrm{v},i}/\xi_{\mathrm{v,eq},i}$ the saturation ratio, σ_p the particle's surface tension, and $v_{\mathrm{m},i}$ the molecular volume. The equilibrium term E reflects the influence of the Kelvin effect. Formula (8) assumes that the influence of heat transport by latent heat on the growth process can be neglected.

Once the growth rates of the individual species are known, the total growth rate is given by $\mathrm{d}m_\mathrm{p}/\mathrm{d}t = \sum_i (\mathrm{d}m_{\mathrm{m},i}/\mathrm{d}t)$. The time derivatives of the moments due to condensation are then readily evaluated as

$$\left(\frac{\partial M_{1,i,j}}{\partial t}\right)_{\mathrm{cond}} = \int_0^\infty \frac{\mathrm{d}m_{\mathrm{p},i}}{\mathrm{d}t}\, n_{\mathrm{LN},j}(m_\mathrm{p})\,\mathrm{d}m_\mathrm{p}\,, \tag{9a}$$

$$\left(\frac{\partial M_{k,j}}{\partial t}\right)_{\mathrm{cond}} = k\int_0^\infty \frac{\mathrm{d}m_\mathrm{p}}{\mathrm{d}t}\, m_\mathrm{p}^{k-1}\, n_{\mathrm{LN},j}(m_\mathrm{p})\,\mathrm{d}m_\mathrm{p}\,. \tag{9b}$$

2.3.2. *Homogeneous nucleation.* In the model presented here, only homogeneous nucleation of one component (denoted by species 1) is taken into account. Nucleation theories predict the formation of nuclei of the critical size $d_\mathrm{p}^* = (4\sigma_1 v_{m,1})/(k_B T \ln S_1)$ at a certain rate J. When d_p^* and J are known, the time derivatives of the moments can be expressed as follows:

$$\left(\frac{\partial M_{1,i,j}}{\partial t}\right)_{\mathrm{nuc}} = \begin{cases} \dfrac{\pi\rho_1}{6}(d_\mathrm{p}^*)^3 J & \text{if } i = 1, \\ 0 & \text{if } i \neq 1, \end{cases} \tag{10a}$$

$$\left(\frac{\partial M_{k,j}}{\partial t}\right)_{\mathrm{nuc}} = \left(\frac{\pi\rho_1}{6}(d_\mathrm{p}^*)^3\right)^k J\,. \tag{10b}$$

It is well known that the discrepancies between different homogeneous nucleation theories are enormous; their results may differ up to a factor 10^{20} (Springer, 1978). In our model, the classical expressions by Frenkel and Becker–Döring and the modified classical nucleation rate by Girshick *et al.* (1990) have been employed. Frenkel's expression for the classical rate is (Frenkel, 1955)

$$J_{\mathrm{Fr}} = \frac{(\rho_\mathrm{g}\xi_{\mathrm{v},1})^2}{\rho_1 m_{\mathrm{m},1}}\sqrt{\frac{2\sigma_1}{\pi m_{\mathrm{m},1}}}\exp\left(-\frac{\pi\sigma_1 (d_\mathrm{p}^*)^2}{3k_\mathrm{B}T}\right). \tag{11}$$

The nucleation rate according to Becker and Döring (1935) is

$$J_{\mathrm{BD}} = (g^*)^{-2/3} J_{\mathrm{Fr}}, \tag{12}$$

where g^* denotes the number of molecules in the critical nucleus. The modified "kinetic" nucleation rate according to Girshick *et al.* (1990) is related to Frenkel's expression by the equation

$$J_{\mathrm{Gi}} = \frac{1}{S_1}\cdot\exp\left(\frac{\sqrt[3]{36\pi v_{\mathrm{m},1}^2}\,\sigma_1}{k_\mathrm{B}T}\right)\cdot J_{\mathrm{Fr}}. \tag{13}$$

2.4. *Numerical procedure*

In order to describe the dynamics of an aerosol reactor, the heat and momentum transport equations in the flow field must be solved simultaneously with the MDE for the moments of all modes and the mass conservation equation for the condensable substances:

$$\frac{\partial \rho_\mathrm{g}\xi_{\mathrm{v},i}}{\partial t} = -\nabla\cdot\mathbf{u}_\mathrm{g}\rho_\mathrm{g}\xi_{\mathrm{v},i} + \nabla\cdot(\rho_\mathrm{g}D_{\mathrm{m},i}\nabla\xi_{\mathrm{v},i}) - \sum_j\left(\frac{\partial \rho_\mathrm{g}M_{1,i,j}}{\partial t}\right)_{\mathrm{cond/nuc}}, \tag{14}$$

where the last term represents gas-to-particle mass transport.

For the solution of this problem, the SIMPLER algorithm (Patankar, 1980) for numerical heat transfer and fluid flow problems is used. The algorithm has been extended to account for particle transport by external forces (Stratmann and Whitby, 1989). It solves systems of equations of the general form

$$\frac{\partial \rho_g \phi_\kappa}{\partial t} + \nabla \cdot (\mathbf{u}_\kappa \rho_g \phi_\kappa) = \nabla \cdot \Gamma_\kappa \nabla \phi_\kappa + (S_{\text{int}})_\kappa, \quad \kappa = 1, \ldots, \nu . \tag{15}$$

ϕ_κ, $\kappa = 1, \ldots, \nu$ are the "independent variables" of the problem, $\mathbf{c}_\kappa$, Γ_κ and $(S_{\text{int}})_\kappa$ denote the related generalized external velocities, diffusivities and internal source terms, respectively. Since the underlying geometry in the problems treated in this article is axisymmetric, the calculations are performed on a 2-D grid with cylindrical coordinates r and z for the radial and axial direction.

The gas flow was assumed to be compressible in the sense that the thermodynamic properties of the gas are temperature dependent. As latent-heat release may be neglected for Dibutylphtalate (Barrett and Fissan, 1989), it is possible to solve the equations for convection and heat transfer separately and use the result as input for the aerosol dynamics problem.

During the calculations, many integrals like those in equation (4) or equation (9) have to be evaluated. A Gauss–Hermite integration procedure is used for this purpose, profiting from the fact that these integrals can be written as integrals over a normal distribution function. This procedure is very accurate as long as the integrands can be "well-approximated by polynomials" of $\ln m_p$ (Press *et al.*, 1992).

3. SIMULATED EXPERIMENTS

In the article of Nguyen *et al.* (1987), extensive measurements on LFARs are compiled. The authors present two slightly differing LFAR setups called system A and system B. System B incorporates an improved saturator and a seed aerosol preparation system and provides better temperature control; we will therefore focus on the results of this setup. Figure 1 shows the schematic setup of the experiment. A gas flow carrying vapor of a condensable substance—here, dibutylphtalate (DBP)—is conducted into a vertical tube which is heated to a constant temperature in its upper part and cooled in its lower part (the condenser). If heat conduction is faster than vapor diffusion, the rapid temperature drop leads to high supersaturations in the tube center. At sufficiently high superstaturations, particles are formed by homogeneous nucleation and start growing by condensation. The resulting aerosol is sampled and measured at the end of the tube. As an extension of this setup, a seed aerosol may be added to the carrier gas in order to examine heterogeneous nucleation.

The carrier gas in system B is dry air. The seed aerosol consists of sodium chloride particles; it is made monodisperse by means of a differential mobility analyzer (DMA). The saturator temperature T_{sat} is equal to the temperature T_{in} of the hot part of the tube. The residence time of the flow in the tube is short enough that, in the simulation, coagulation can be neglected for particle concentrations below 10^6 cm^{-3}. As a further simplification to the model, the sodium chloride particles may be considered inert under the given conditions; therefore gas-to-particle conversion needs to be considered for the dibutylphtalate component only, and mixing inside the droplets may be neglected.

In our simulations, a unimodal approach was used for the homogeneous nucleation experiments and a bimodal model with two chemical components for the heterogeneous case. The multicomponent model prevented evaporation of the seed particles in the calculation and made the algorithm thereby more exact and, in particular, more stable. Table 1 shows the correspondences of the independent variables in the model with the general terms in the equation system (15). At the tube inlet, the boundary conditions are as follows: a laminar profile for the gas velocity; $T = T_{\text{in}}$; $\xi_{v,\text{DBP}} = \xi_{v,\text{DBP,eq}}(T_{\text{in}})$; and the size distribution moments are set to 0 for the nucleation mode and to those of the seed aerosol

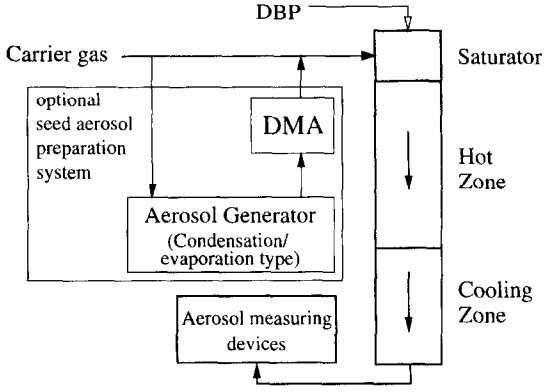

Fig. 1. Schematic setup of the LFAR of Nguyen *et al.* (1987) (system B). DBP—dibutylphtalate; DMA—differential mobility analyzer.

Table 1. Correspondences of the physical variables and the general terms of equation (15)

ϕ	$\mathbf{u}_z$	$\mathbf{u}_r$	Γ	S_{int}
$(\mathbf{u}_g)_z$	$(\mathbf{u}_g)_z$	$(\mathbf{u}_g)_r$	μ_g	AVT
$(\mathbf{u}_g)_r$	$(\mathbf{u}_g)_z$	$(\mathbf{u}_g)_r$	μ_g	AVT
T	$(\mathbf{u}_g)_z$	$(\mathbf{u}_g)_r$	k_g/c_p	0
$\xi_{v,\text{DBP}}$	$(\mathbf{u}_g)_z$	$(\mathbf{u}_g)_r$	$\rho_g D_{m,\text{DBP}}$	$-\rho_g \sum_j \left(\frac{\partial M_{1,\text{DBP},j}}{\partial t}\right)_{c/n}$
$M_{1,\text{DBP},j}$	$(\mathbf{u}_{1,j})_z$	$(\mathbf{u}_{1,j})_r$	$\rho_g D_{1,j}$	$\rho_g \left(\frac{\partial M_{1,\text{DBP},j}}{\partial t}\right)_{c/n}$
$M_{1,\text{N},j}$	$(\mathbf{u}_{1,j})_z$	$(\mathbf{u}_{1,j})_r$	$\rho_g D_{1,j}$	0
$M_{k,j}$, $k = 0,2$	$(\mathbf{u}_{k,j})_z$	$(\mathbf{u}_{k,j})_r$	$\rho_g D_{k,j}$	$\rho_g \left(\frac{\partial M_{k,j}}{\partial t}\right)_{c/n}$

Note: c_p is the specific heat capacity of the gas. AVT — additional viscosity terms. $\mathbf{u}_{k,j}$ stands for $\mathbf{u}_g + \mathbf{c}_{k,j}$. Indices: DBP for dibutylphtalate, N for NaCl, c/n for the internal processes condensation and nucleation.

for the other mode. The boundary condition for the temperature at the tube wall is discussed in Section 4.3.2; the vapor concentration at the wall is set to the equilibrium concentration at the wall temperature. All other variables are set to 0 at the tube wall.

Problems involving nucleation require high axial grid resolutions. In the calculations presented here, irregular grids with 400–1000 axial and 20–60 radial grid points have been used, leading to a maximal spatial resolution of 0.2 mm (axial) resp. 0.05 mm (radial) in the nucleation zone.

The physico-chemical properties of dibutylphtalate were taken from the article of Nguyen *et al.* and those of the other substances from standard textbooks.

4. RESULTS

4.1. *Reference case*

In this section, measured data and simulations will be presented for a fixed set of experimental and modeling parameters that will be called the "reference case". For the selected experimental parameters (condenser temperature $T_c = 22°C$ and gas flux $Q = 0.5\,\text{l}\,\text{min}^{-1}$), a large amount of measurement data is presented in Nguyen *et al.* (1987), including a wall-temperature profile for the inlet temperature $T_{in} = 99°C$. This wall-temperature profile was used as wall boundary condition for the simulations, assuming that the relative wall-temperature profile $(T_w - T_c)/(T_{in} - T_c)$ does not change if T_{in} is varied. The nucleation rate by Girshick *et al.* was employed; it was corrected with a constant factor

$c_{nuc} = 10^{-3}$. Correction factors of this kind are widely used because of the high uncertainties in the absolute values of nucleation rates. Figure 2 shows the simulation results and the experimental data for the homogeneous nucleation experiment. The number concentration of particles at the outlet $\rho_g N_{out}$ (by convention, all figures show volume-based concentrations $\rho_g N$ instead of the mass-based concentrations N used in the calculations) is plotted against the saturator temperature T_{sat} that determines the mass concentration of dibutylphtalate vapor in the system. The deviations between measurement and simulation are less than 20% for saturator temperatures between 90 and 100°C.

Figure 3 shows the dependence of $\rho_g N_{out}$ on the seed aerosol concentration $\rho_g N_s$ (for consistency with Nguyen *et al.*, $\rho_g N_s$ is the number concentration of seed particles at the tube outlet) in the reference case for heterogeneous nucleation. The experimental parameters and the nucleation rate are the same as in the homogeneous case. The inlet temperature $T_{in} = T_{sat}$ is 99°C. The diameter of the seed particles is 43.3 nm. Figure 3 also contains the simulation results presented by Nguyen *et al.* as well as those calculated by Phanse and Pratsinis (1989) using their dimensionless unimodal lognormal model.

All curves in Fig. 3 show the same principal behaviour: for low seed aerosol concentrations, $\rho_g N_{out}$ is close to its value $\rho_g N_{hom}$ for homogeneous nucleation (in this case the experimental value for $\rho_g N_{hom}$ is 1.05×10^5 cm^{-3}). When the seed concentration is increased, vapor is scavenged by the seed particles, leading to a decrease of the number of nucleated particles for $\rho_g N_s \geqslant 5 \times 10^4$ cm^{-3}, nucleation is completely suppressed and $N_{out} = N_s$. However, the experimentally observed suppression of nucleation at intermediate seed aerosol concentrations is less pronounced than the simulations predict (see Section 5.2). The simulation results of the model presented here and those from Nguyen *et al.* (1987) are in astonishing agreement in view of the fact that the modeling technique by Peshty *et al.* (1983) is entirely different from the modal technique.

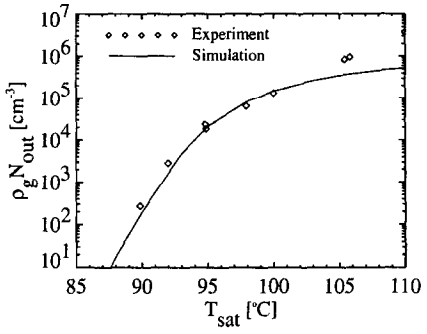

Fig. 2. Results for the "reference case" for homogeneous nucleation. Number concentration of particles at the tube outlet $\rho_g N_{out}$ versus saturator temperature T_{sat}.

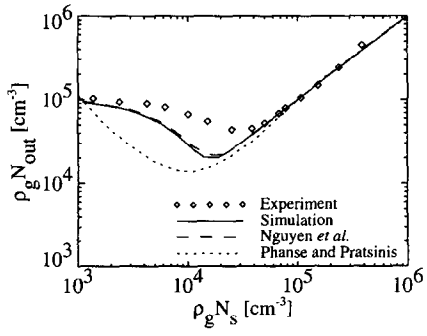

Fig. 3. Dependence of $\rho_g N_{out}$ on the seed aerosol concentration $\rho_g N_s$ in the "reference case" for heterogeneous nucleation.

Before proceeding in our analysis, we will now give a survey of the model output and provide some insight into the dynamics of the system.

4.2. *Model output*

Figure 4 shows two-dimensional profiles of important variables of the system for heterogeneous nucleation with $\rho_g N_s = 10^4\ \mathrm{cm}^{-3}$ in the reference case.

The upper part of the figure shows the thermodynamic variables temperature (T), vapor mass concentration ($\rho_g \xi_v$) and saturation ratio (S). $z = 0$ has been set to the axial position at which the wall temperature has dropped to its cooling zone value T_c. The vapor concentration decreases rapidly close to the tube wall ($r = 5$ mm) because of condensation to the wall. This causes the saturation ratio S in this region to stay below 200, whereas it rises to values greater than 600 in the tube center. At this high supersaturation, nucleation becomes significant. Comparison with the lower left plot in the figure shows the increase of the particle number concentration $\rho_g M_0$ in this "nucleation zone", which extends about 50 mm in the axial direction and 1.5 mm in the radial direction. Before the onset of nucleation, the number concentration equals the seed aerosol concentration $\rho_g N_s$.

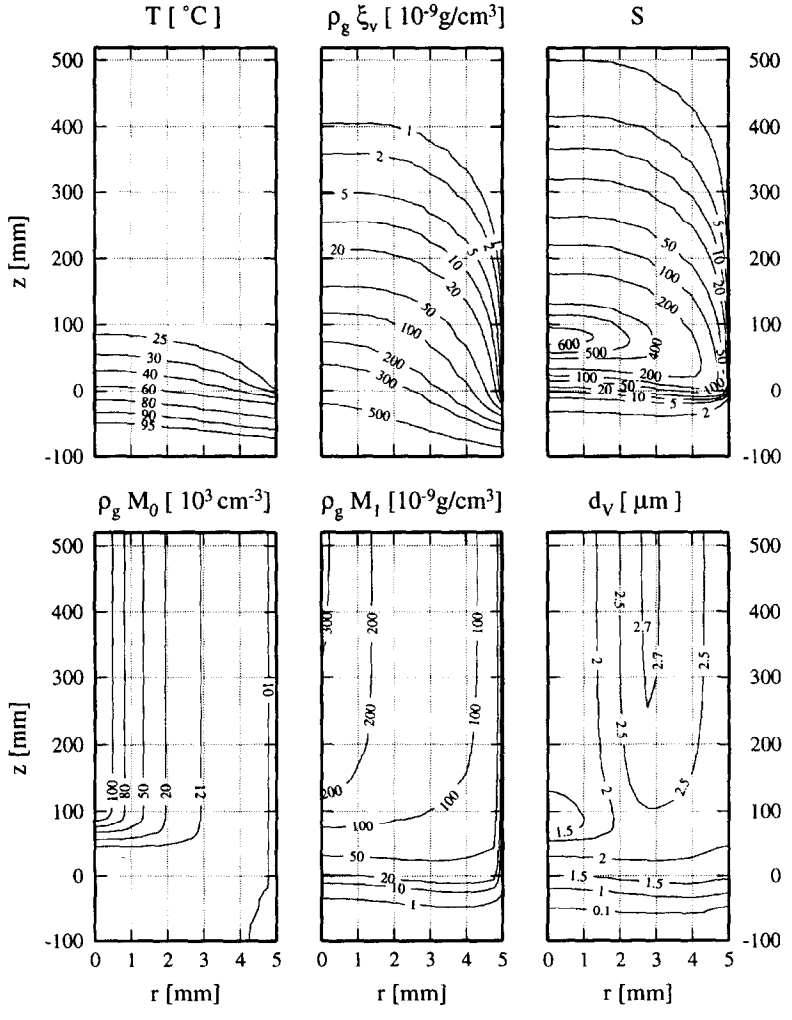

Fig. 4. Two-dimensional profiles of important thermodynamic and aerosol dynamic variables in the flow tube for experiment B.

The figure in the center bottom shows the aerosol mass concentration $\rho_g M_1$. A comparison with the vapor concentration profile in the plot above illustrates the transfer of dibutylphtalate from the vapor to the particles and its depressing effect on nucleation: In the nucleation zone, the particle mass concentration is about 100 mg m^{-3}. This is the amount of vapor that has condensed to the seed particles before the onset of nucleation. In the absence of seed aerosol, the vapor concentration in this part of the tube would be approximately 100 mg m^{-3} higher, leading to a much higher supersaturation and, consequently, a higher nucleation rate.

The right figure at the bottom shows a profile of the volume mean diameter d_V (the diameter corresponding to the mean particle volume of the total aerosol distribution). The seed particles grow very quickly from their initial size of 43.3 nm to about 2 μm. The mean particle size decreases in the nucleation zone because the nucleated particles are small. The largest mean particle size is found at a radial distance of *ca.* 3 mm from the centerline.

Figure 5 visualizes the resulting mixing-cup average size distribution

$$\left\langle \rho_g \frac{dN}{d(\ln d_p)} \right\rangle = \frac{\int_0^R \rho_g (dN/d(\ln d_p))\,|_r \cdot 2\pi (\mathbf{u}_g)_z r\, dr}{\int_0^R 2\pi (\mathbf{u}_g)_z r\, dr} \tag{16}$$

at different downstream locations for the same operating conditions as in Fig. 4. The size distribution remains bimodal throughout the tube, because the amount of vapor does not suffice to let the nucleated particles grow to the same size as the seed particles.

4.3. *Influence of various model assumptions*

In this section we will examine the sensitivity of the model to different assumptions that deviate from those described in Section 4.1.

Figure 6 summarizes the effect of some simplifying assumptions on the results of the simulation for heterogeneous nucleation. As in Fig. 3, the dependence of $\rho_g N_{out}$ on $\rho_g N_s$ is plotted in the figure. Neglect of thermophoresis and diffusion (dashed line) turns out to have almost no effect on the model results; the same holds for the Kelvin effect (dash-dotted line).

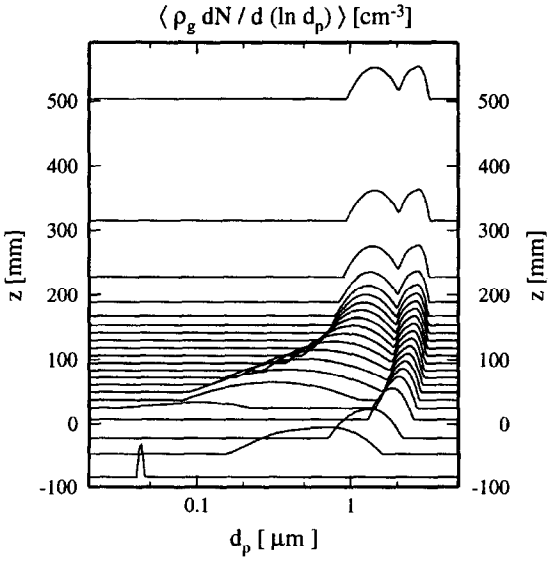

Fig. 5. Evolution of the mixing-cup averaged size distribution. The distributions are plotted logarithmically and truncated to a lower bound of 0.1 cm^{-3}.

If the bimodal model is replaced by a unimodal one (dotted line), a deviation can be seen for those seed aerosol concentrations at which both modes (seed aerosol and nucleated particles) contribute significantly to the total number of particles. As expected, the deviations become small for very high and very low seed aerosol concentrations, at which the number concentration in one of the modes is very small compared with the other one.

4.3.1. *Nucleation rate.* Figure 7 shows the dependence of $\rho_g N_{out}$ on $\rho_g N_s$ for different nucleation rate expressions. Under the given conditions, the classical nucleation rates are about seven orders of magnitude lower than the nucleation rate according to Girshick *et al.* (1990). Thus, the correction factors c_{nuc} have to be adjusted for each nucleation rate expression to yield the correct number of nucleated particles in the case of homogeneous nucleation. If this is done, the functions $\rho_g N_{out}(\rho_g N_s)$ for heterogeneous nucleation are practically identical to the reference case for both classical nucleation rates. This is not a trivial result, because the three nucleation rate expressions, apart from giving different absolute values, also have a different dependence on saturation ratio and temperature.

4.3.2. *Wall temperature profile.* The temperature field inside the tube determines the supersaturation and, thereby, nucleation and condensation rates. It is therefore crucial for the simulation to apply correct boundary conditions for the temperature field.

In this paper, different wall temperature profiles were used: (a) the measured profile, as taken from Nguyen *et al.*, interpolated with cubic splines (also used in the reference case); (b) an idealized stepwise profile; (c) the linearly interpolated profile as used in Phanse and Pratsinis (1989). These profiles are illustrated in the left panel of Fig. 8 for $T_{in} = 99°C$, $T_{out} = 22°C$ and $Q = 0.5\,l\,min^{-1}$. In the right part of the figure, the centerline temperatures

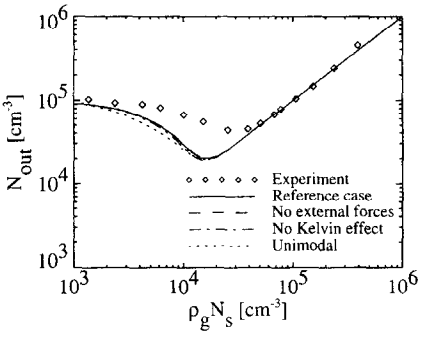

Fig. 6. The "reference case" simulation for heterogeneous nucleation compared with some simplified calculations.

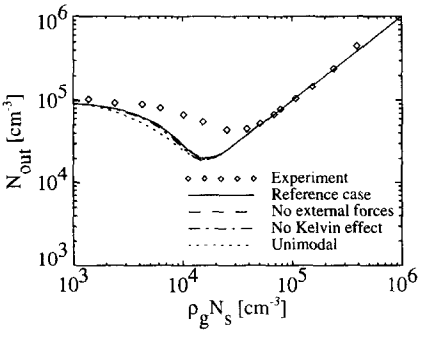

Fig. 7. Comparison of the "reference case" simulation for heterogeneous nucleation with simulations using the nucleation rates by Frenkel and Becker–Döring in combination with adequate correction factors that are indicated in the figure.

resulting from these assumptions are shown and compared with the measured and calculated centerline profiles from Nguyen *et al.* (1987). The centerline profile calculated from assumption (a) agrees well with the calculated profile from Nguyen *et al.* (deviation $\leqslant 1°C$). The authors claim that the latter curve and the measured centerline profile agree "within experimental error". As can bee seen in Fig. 8, both the linear and the stepwise wall temperature profile produce a poorer agreement to the centerline measurements than the interpolated one. Nevertheless, the "experimental error" may apply equally well to the wall temperatures as to those at the centerline, and the wall boundary condition must be regarded as an approximation.

The stepwise and linear profiles can be thought of as extreme cases giving an upper bound to the possible errors due to erroneous boundary conditions at the wall in the simulation. The results of simulations with different wall temperature profiles are shown in Fig. 9. Girshick's nucleation rate with $c_{nuc} = 10^{-3}$ was employed in all cases. The stepwise profile results in a much higher particle production than the measured one, whereas the linear profile leads to lower particle numbers. Particle production increases in general if the wall temperature profile becomes steeper, because the saturation ratio rises faster, leaving less time for the vapor to condense to the walls or seed particles before the onset of nucleation.

It is obvious from Fig. 9 that LFAR models are very sensitive to the choice of the wall temperature profile in the transition zone. The method of using a linear or stepwise approximation, which has been applied frequently in the literature, leads to deviations of particle numbers up to an order of magnitude. The same sensitivity to changes in the wall temperature profile should be expected in LFAR experiments. Experimentalists should take great care to provide stable and exactly measured profiles for such setups.

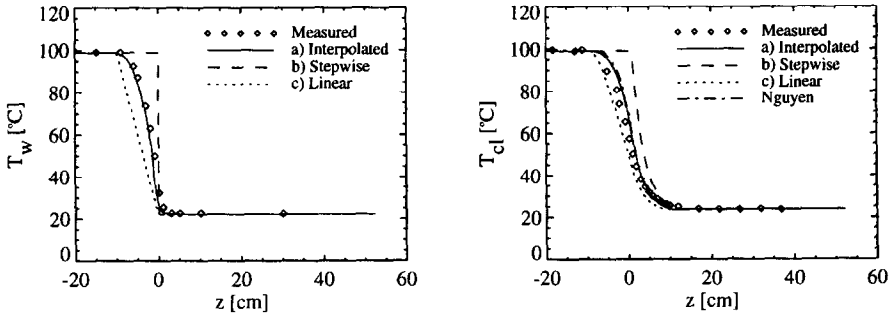

Fig. 8. Axial profiles of the wall temperature T_w (left) and corresponding centerline temperature T_{cl} (right).

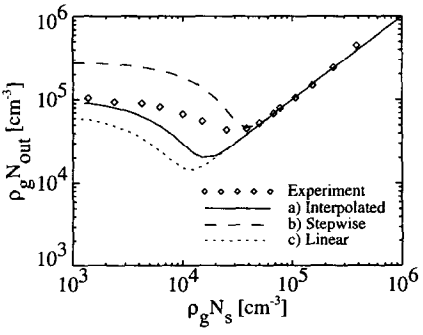

Fig. 9. Comparison of the "reference case" simulation for heterogeneous nucleation with similar calculations using the stepwise and linear wall temperature profile, respectively.

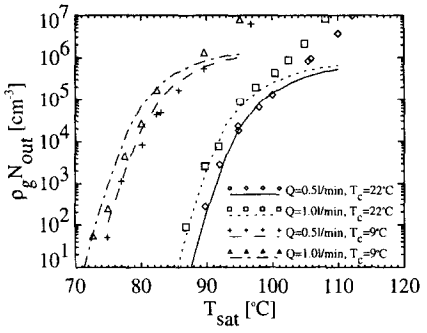

Fig. 10. Homogeneous nucleation experiments for system B from Nguyen *et al.* (1987) for different gas flow rates Q and wall temperatures T_c and the respective simulation results.

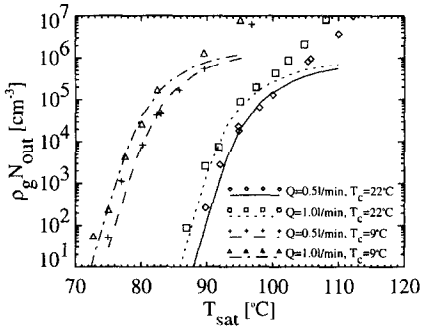

Fig. 11. As in Fig. 10, but with Frenkel's nucleation rate.

4.4. *Variation of the experimental parameters*

As a further test of the performance of the model, its results were compared with experimental data for different values of the condenser wall temperature T_c and the flow rate Q. Figure 10 presents all homogeneous nucleation measurements presented by Nguyen *et al.* for system B. The agreement is of course the best for $Q = 0.5\,\mathrm{l\,min^{-1}}$ and $T_c = 22°C$, because the correction factor $c_{nuc} = 10^{-3}$ has been adjusted to fit this curve. Nevertheless, the agreement for the other parameter values is also satisfying.

Surprisingly, the overall agreement between simulation and experiment becomes even better if Frenkel's nucleation rate is employed with the suitable correction factor $c_{nuc} = 10^4$ (see Section 4.3.1). These results are shown in Fig. 11.

It should be highlighted that good agreement between measurement and calculation is obtained using the same factor for all parameter values. In earlier publications, on the contrary, the correction factors used to vary by several orders of magnitude for different sets of experimental parameters (e.g. Nguyen *et al.*, 1987).

5. DISCUSSION

5.1. *Nucleation correction factors*

As stated in Section 4.3.1, a correction factor of 10^4 was used for Frenkel's nucleation rate. This is a much lower value than the one obtained by Nguyen *et al.* (1987) with Peshty's model: Their curve in Fig. 2 was calculated with $c_{nuc} = 2.5 \times 10^6$. Unfortunately, Peshty's model and especially the calculations presented in the paper of Nguyen *et al.* are not documented in sufficient detail to examine the reason for this deviation. The nucleation factors (called enhancement factors) in their paper vary between 4×10^4 and 6×10^7 for simulations at different operating conditions.

Phanse and Pratsinis (1989) have obtained $c_{nuc} = 10^6$ with a linear temperature profile and the nucleation rate of Becker–Döring. This is consistent with our results: If our model is run with the same assumptions, the same optimal value for the correction factor is obtained.

5.2. *Deviations from the experimental results*

As shown in the previous section, the predicted number concentrations of our model agree reasonably well with the experimental data of Nguyen *et al.* However, in some instances the agreement is poor: (1) Figures 10 and 11 show that in our model the number concentration levels off at high inlet temperatures, an effect that cannot be seen in the experimental data; (2) the depressing effect of the seed aerosol on nucleation is overpredicted (see Fig. 3).

It is important to note that these shortcomings are not particular to our model, but have also been observed by Nguyen *et al.* and Phanse and Pratsinis. Since Peshty's model is general with respect to the size distribution, the deviations can probably not be attributed to the modal modeling technique.

In the following, we will consider the case of heterogeneous nucleation. If experimental errors can be excluded (which is highly probable, since the deviations between theory and experiment amount to a factor of 3), some of the model parameters must be erroneous. The only parameter examined in Section 4.3 with a considerable influence on the results was the wall-temperature profile. The depression of nucleation by the seed aerosol is in fact slightly lower when a steeper wall temperature profile (e.g. the stepwise profile of Section 4.3.2) is employed. However, this effect is not strong enough to explain the observed deviations.

Since the homogeneous nucleation results are very good in the parameter range of the heterogeneous nucleation experiment, and the choice of the nucleation rate has almost no influence on the simulation outcome (cf. Fig. 7), it is unlikely that the problem could be solved by employing a different nucleation rate. A simple reasoning suggests that the seed aerosol effect is due to condensation, and the reason for the deviations may therefore be that *the loss of vapor through condensation is overestimated.* This could have several causes, e.g. inaccurate assumptions about the vapor pressure or diffusivity of dibutylphtalate. A simple numerical investigation was carried out by introducing a constant "condensation correction factor" c_{cond} to equation (8) and adjusting c_{nuc} such that the correct results are obtained for homogeneous nucleation. Fig. 12 shows the results obtained with $c_{cond} = 0.4$ and $c_{nuc} = 5 \times 10^{-4}$ using Girshick's nucleation rate expression. The simulation results match the measurement data very well in this case. However, the overall agreement for homogeneous nucleation under different operating conditions deteriorates with respect to the reference case simulation. An unequivocal correction factor for condensation cannot be derived from the data at hand, nor is it possible to give a satisfactory physical interpretation of this correction. Nevertheless, a future discussion of this topic might be fruitful.

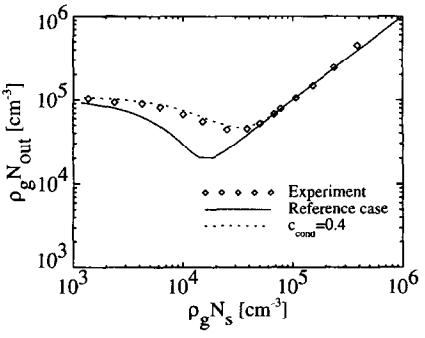

Fig. 12. Simulation of the heterogeneous nucleation experiment with an "condensation correction factor" $c_{cond} = 0.4$ compared to the experimental data and the reference case simulation.

6. SUMMARY

The MADMAcS 1 code provides a bimodal lognormal multicomponent aerosol model that calculates the mode-average particle composition. It is sufficiently general and fast to be applied in a variety of two- and three-dimensional problems. As a first application, the model has been tested for a laminar flow aerosol reactor setup. Comparison with experimental data shows satisfying agreement over a wide range of experimental parameters with the same nucleation rate expression.

If suitable correction factors are applied, the classical nucleation rates given by Frenkel and Becker–Döring and the modified classical nucleation theory by Girshick *et al.* (1990) match the data equally well. A discrimination between different nucleation theories can therefore only be expected from an experiment of this type if the measurements are carried out at a high variety of operating conditions. Furthermore, the temperature profiles at the tube wall must be determined very carefully in order to facilitate a reasonable comparison between simulations and experimental data.

For heterogeneous nucleation, the simulation results show the same deviations from experimental data as previously published model calculations. It is suggested that this may be due to an overestimation of the rate of vapor condensation to the seed aerosol.

Acknowledgements—Figures 4 and 5 were prepared with the public domain graphics software GMT from the university of Hawaii (Wessel and Smith, 1991).

REFERENCES

Anisimov, M. P. and Hämeri, K. and Kulmala, M. (1994) Construction and test of laminar flow diffusion chamber: homogeneous nucleation of DBP and *n*-hexanol. *J. Aerosol Sci.* **25,** 23–32.

Barrett, J. C. and Fissan, H. (1989) Wall and aerosol condensation during cooled laminar tube flows. *J. Colloid Interface Sci.* **130,** 498–507.

Becker, R. and Döring, W. (1935) Kinetische Behandlung der Keimbildung in übersättigten Dämpfen, *Ann. Phys. (Leipzig)* [5] **24,** 719–752.

Brock, J. R., Kuhn, P. J. and Zehavi, D. (1988) Formation and growth of binary aerosol in a laminar coaxial jet. *J. Aerosol Sci.* **19,** 413–424.

Frenkel, J. (1955) *Kinetic Theory of Liquids.* Dover, New York.

Friedlander, S. K. (1977) *Smoke, Dust and Haze.* Wiley, New York.

Fuchs, N. A. and Sutugin, A. G. (1971) Highly dispersed aerosols. In *Topics in Current Aerosol Research* (Edited by Hidy, G. M. and Brock, J. R.), pp. 1–60. Pergamon, Oxford.

Girshick, E. R. and Chiu, C.-P. and McMurry, P. H. (1990) Time-dependent aerosol models and homogeneous nucleation rates. *Aerosol Sci. Technol.* **13,** 465–477.

Hämeri, K., Kulmala, M. and Rantanen, E. (1995) Homogeneous nucleation of DBP vapour in a laminar flow diffusion chamber: the carrier gas effect. *J. Aerosol Sci.* **26,** S631–S632.

Nguyen, H. V., Okuyama, K., Mimura, T., Kousaka, Y., Flagan, R. C. and Seinfeld, J. H. (1987) Homogeneous and heterogeneous nucleation in a laminar flow aerosol reactor. *J. Colloid Interface Sci.* **119,** 491–504.

Patankar, S. V. (1980) *Numerical Heat Transfer and Fluid Flow.* McGraw–Hill, New York.

Peshty, A. J. and Flagan, R. C. and Seinfeld, J. H. (1983) Theory of aerosol formation and growth in laminar flow. *J. Colloid Interface Sci.* **91,** 525–545.

Phanse, G. M. and Pratsinis, S. E. (1989) Theory of aerosol generation in laminar flow condensers. *Aerosol Sci. Technol.* **11,** 100–118.

Press, W. H., Teukolsky, S. A., Vetterling, W. T. and Flannery, B. P. (1992) *Numerical Recipes in FORTRAN*, 2nd Edition. Cambridge University Press, Cambridge.

Springer, G. S. (1978) Homogeneous nucleation. *Adv. Heat Transfer* **14,** 281–346.

Stratmann, F. and Whitby, E. R. (1989) Numerical solution of aerosol dynamics for simultaneous convection, diffusion and external forces. *J. Aerosol Sci.* **20,** 437–440.

Talbot, L., Cheng, R. K., Schefer, R. W. and Willis, D. (1980) Thermophoresis in a heated boundary layer. *J. Fluid Mech.* **101,** 737–758.

Wessel, P. and Smith, W. H. F. (1991) Free software helps map and display data. *EOS Trans. Amer. Geophys. U.* **72,** 441, 445–446.

Whitby, E. R. (1989) Modal aerosol dynamics modeling. Ph.D. thesis, University of Minnesota, Minneapolis.

Whitby, E. R. and McMurry, P. H., Shankar, U. and Binkowski, F. S. (1991) Modal aerosol dynamics modeling. Technical Report, U.S. Environmental Protection Agency, Research Triangle Park, NC 27711.